

Symmetry breaking and Wigner molecules in few-electron quantum dots

Constantine Yannouleas* and Uzi Landman**

School of Physics, Georgia Institute of Technology, Atlanta, GA 30332-0430

Received zzz, revised zzz, accepted zzz

Published online zzz

PACS 73.21.La,73.22.Gk,73.63.Kv,73.43.-f,67.80.Cx,03.67.Mn

[Invited talk at TNT2005 (Trends in Nanotechnology), *Physica status solidi (a)* 203, 1160 (2006)]

We discuss symmetry breaking in two-dimensional quantum dots resulting from strong interelectron repulsion relative to the zero-point kinetic energy associated with the confining potential. Such symmetry breaking leads to the emergence of crystalline arrangements of electrons in the dot. The so-called Wigner molecules form already at field-free conditions. The appearance of rotating Wigner molecules in circular dots under high magnetic field, and their relation to magic angular momenta and quantum-Hall-effect fractional fillings is also discussed. Recent calculations for two electrons in an elliptic quantum dot, using exact diagonalization and an approximate generalized-Heitler-London treatment, show that the electrons can localize and form a molecular dimer for screened interelectron repulsion. The calculated singlet-triplet splitting (J) as a function of the magnetic field (B) agrees with cotunneling measurements; its behavior reflects the effective dissociation of the dimer for large B . Knowledge of the dot shape and of $J(B)$ allows determination of two measures of entanglement (concurrence and von Neumann entropy for *indistinguishable* fermions), whose behavior correlates also with the dissociation of the dimer. The theoretical value for the concurrence at $B = 0$ agrees with the experimental estimates.

Copyright line will be provided by the publisher

1 Symmetry breaking in quantum dots

Two-dimensional (2D) quantum dots (QDs), created at semiconductor interfaces through the use of lithographic and gate-voltage techniques, with refined control of their size, shape, and number of electrons, are often referred to as “artificial atoms” [1, 2, 3]. These systems which, with the use of applied magnetic fields, are expected to have future applications as nanoscale logic gates and switching devices, have been in recent years the subject of significant theoretical and experimental research efforts. As indicated above, certain analogies have been made between these man-made systems and their natural counterparts, suggesting that the physics of electrons in the former is similar to that underlying the traditional description of natural atoms – pertaining particularly to electronic shells and the Aufbau principle in atoms (where electrons are taken to be moving in a spherically averaged effective central mean-field potential).

The above-mentioned analogy has been theoretically challenged recently [4, 5] on the basis of calculations that showed evidence for formation, under favorable conditions (that are readily achieved in the laboratory), of “electron molecules,” which are alternatively called Wigner molecules (WMs) after the physicist who predicted formation of electron crystals in extended systems [6]. These spin-and-space (sS) unrestricted Hartree-Fock (UHF) calculations (denoted in the following as sS-UHF or simply UHF) of electrons confined in 2D QDs by a parabolic external potential led to the discovery of spontaneous symmetry breaking in QDs, manifested in the appearance of distinct interelectronic spatial (crystalline)

* e-mail: Constantine.Yannouleas@physics.gatech.edu

** e-mail: Uzi.Landman@physics.gatech.edu

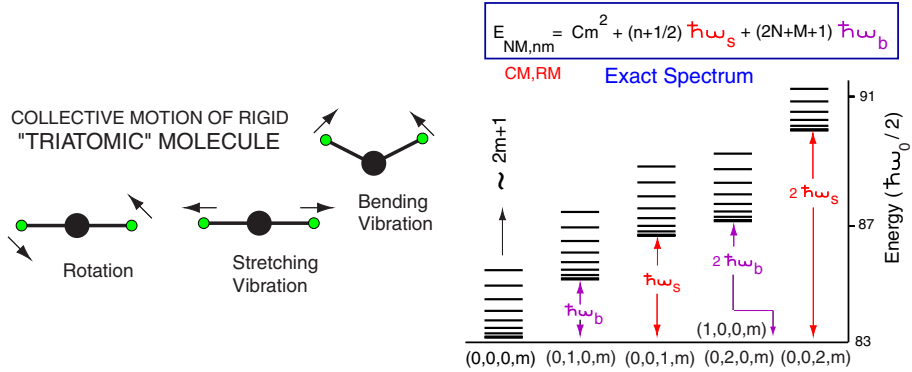


Fig. 1 The calculated spectrum of a two-electron parabolic quantum dot, with $R_W = 200$. The quantum numbers are (N, M, n, m) with N corresponding to the number of radial nodes in the center of mass (CM) wavefunction, and M is the CM azimuthal quantum number. The integers n and m are the corresponding quantum numbers for the electrons' relative motion (RM) and the total energy is given by $E_{NM,nm} = E_{NM}^{cm} + E^{rm}(n, |m|)$. The spectrum may be summarized by the "spectral rule" given in the figure, with $C = 0.037$, the phonon stretching vibration $\hbar\omega_s = 3.50$, and the phonon for the bending vibration coincides with that of the CM motion, i.e., $\hbar\omega_b = \hbar\omega_0 = 2$. All energies are in units of $\hbar\omega_0/2$, where ω_0 is the parabolic confinement frequency.

correlations (even in the absence of magnetic fields). Such symmetry breaking may indeed be expected to occur based on the interplay between the interelectron repulsion, Q , and the zero-point kinetic energy, K . It is customary to take $Q = e^2/\kappa l_0$ and $K \equiv \hbar\omega_0$, where $l_0 = (\hbar/m^*\omega_0)^{1/2}$ is the spatial extent of an electron in the lowest state of the parabolic confinement; m^* is the electron effective mass, κ is the dielectric constant, and ω_0 is the frequency that characterizes the parabolic (harmonic) confining potential. Thus, defining the Wigner parameter as $R_W = Q/K$, one may expect symmetry breaking to occur when the interelectron repulsion dominates, i.e., for $R_W > 1$. Under such circumstances, an appropriate solution of the Schrödinger equation necessitates consideration of wave functions with symmetries that are lower than that of the circularly symmetric QD Hamiltonian. Such solutions may be found through the use of the sS-UHF method, where all restrictions on the symmetries of the wave functions are lifted. On the other hand, when $R_W < 1$, no symmetry breaking is expected, and the sS-UHF solution collapses onto that obtained via the restricted Hartree-Fock (RHF) method, and the aforementioned circularly symmetric "artificial-atom" analogy maintains. From the above we note that the state of the system may be controlled and varied through the choice of materials (i.e., κ) and/or the strength of the confinement (ω_0), since $R_W \propto 1/(\kappa\sqrt{\omega_0})$.

1.1 Two-electron circular dots

To illustrate the formation of "electron molecules," we show first exact results obtained for a two-electron QD, through separation of the center-of-mass and inter-electron relative-distance degrees of freedom [7]. The spectrum obtained for $R_W = 200$ (Fig. 1), exhibits features that are characteristic of a collective rovibrational dynamics, akin to that of a natural "rigid" triatomic molecule with an infinitely heavy middle particle representing the center of mass of the dot. This spectrum transforms to that of a "floppy" molecule for smaller value of R_W (i.e., for stronger confinements characterized by a larger value of ω_0 , and/or for weaker inter-electron repulsion), ultimately converging to the independent-particle picture associated with the circular central mean-field of the QD. Further evidence for the formation of the electron molecule was found through examination of the conditional probability distribution (CPD); that is, the anisotropic pair correlation $P(\mathbf{r}, \mathbf{r}_0)$, which expresses the probability of finding a particle at \mathbf{r} given that the "observer"

(reference point) is riding on another particle at \mathbf{r}_0 [5, 7],

$$P(\mathbf{r}, \mathbf{r}_0) = \langle \Psi | \sum_{i=1}^N \sum_{j \neq i}^N \delta(\mathbf{r}_i - \mathbf{r}) \delta(\mathbf{r}_j - \mathbf{r}_0) | \Psi \rangle / \langle \Psi | \Psi \rangle. \quad (1)$$

Here $\Psi(\mathbf{r}_1, \mathbf{r}_2, \dots, \mathbf{r}_N)$ denotes the many-body wave function under consideration. It is instructive to note here certain similarities between the formation of a “two-electron molecule” in man-made quantum dots, and the collective (rovibrational) features observed in the electronic spectrum of doubly-excited helium atoms [8, 9, 10].

For confined (finite) systems with a larger number of particles, one must resort to approximate computational schemes. Of particular interest are methodologies that permit systematic evaluation of high-accuracy solutions to these many-body strongly-correlated systems, under field-free conditions, as well as under the influence of an applied magnetic field. We remark here, that the relatively large (spatial) size of QDs (resulting from materials’ characteristics, e.g., a small electron effective mass and large dielectric constant), allows the full range of orbital magnetic effects to be covered for magnetic fields that are readily attained in the laboratory (less than 40 T). In contrast, for natural atoms and molecules, magnetic fields of sufficient strength (i.e., larger than 10^5 T) to produce novel phenomena related to orbital magnetism (beyond the perturbative regime), are known to occur only in astrophysical environments (e.g., on the surface of neutron stars).

The 2D hamiltonian of the problem under consideration is given by

$$H = \sum_{i=1}^N \frac{1}{2m^*} \left(\mathbf{p}_i - \frac{e}{c} \mathbf{A}_i \right)^2 + \sum_{i=1}^N \frac{m^*}{2} \omega_0^2 \mathbf{r}_i^2 + \sum_{i=1}^N \sum_{j>i}^N \frac{e^2}{\kappa r_{ij}}, \quad (2)$$

describing N electrons (interacting via a Coulomb repulsion) confined by a parabolic potential of frequency ω_0 and subjected to a perpendicular magnetic field \mathbf{B} , whose vector potential is given in the symmetric gauge by $\mathbf{A}(\mathbf{r}) = \mathbf{B} \times \mathbf{r}/2 = (-By, Bx, 0)/2$. For sufficiently high magnetic field values (i.e., in the fractional quantum Hall effect, or FQHE, regime), the electrons are fully spin-polarized and the Zeeman term (not shown here) does not need to be considered. In the $B \rightarrow \infty$ limit, the external confinement ω_0 can be neglected, and H can be restricted to operate in the lowest Landau level (LLL), reducing to the form [11, 12, 13, 14]

$$H_{\text{LLL}} = N \frac{\hbar \omega_c}{2} + \sum_{i=1}^N \sum_{j>i}^N \frac{e^2}{\kappa r_{ij}}, \quad (3)$$

where $\omega_c = eB/(m^*c)$ is the cyclotron frequency.

For finite N , the solutions to the Schrödinger equations corresponding to the hamiltonians given by Eq(2) (with or without a magnetic field), or by Eq(3) (in the $B \rightarrow \infty$ limit), must have a good angular momentum, L , and good spin quantum numbers (the latter is guaranteed in the high B , fully spin-polarized case). As described in detail elsewhere [11, 12, 13, 14, 15, 16], these solutions can be well approximated by a two-step method consisting of symmetry breaking at the spin-and-space unrestricted Hartree-Fock level and subsequent symmetry restoration via post-Hartree-Fock projection techniques. We recall that the sS-UHF method relaxes both the double-occupancy requirement (namely, different spatial orbitals are employed for different spin directions), as well as relaxing the requirement that the electron (spatial) orbitals be constrained by the symmetry of the external confining potential.

Results obtained for various approximation levels for a two-electron QD with $B = 0$ and $R_W = 2.40$ (that is, in the Wigner-molecule regime) are displayed in Fig. 2. In these calculations [16], the spin projection was performed following reference [17], i.e., one constructs the wave function

$$\Psi_{\text{SP}}(s) = \mathcal{P}_{\text{spin}}(s) \Psi_{\text{UHF}}, \quad (4)$$

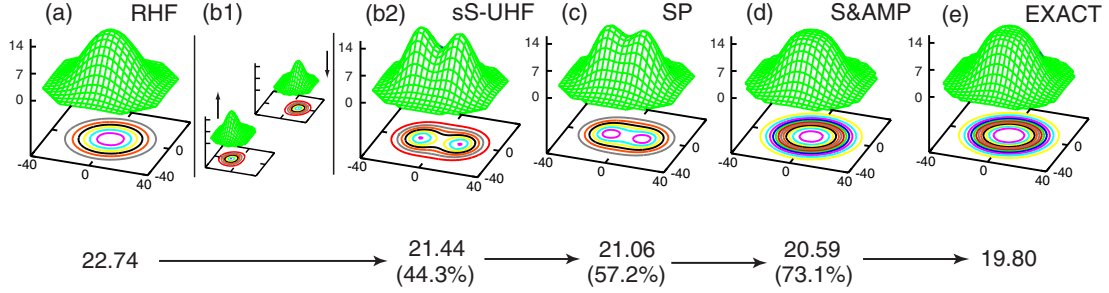


Fig. 2 Various approximation levels for a field-free two-electron QD with $R_W = 2.40$. (a) Electron density of the RHF solution, exhibiting circular symmetry (due to the imposed symmetry restriction). The correlation energy $\epsilon_c = 2.94$ meV, is defined as the difference between the energy of this state and the exact solution [shown in frame (e)]. (b1) and (b2) The two occupied orbitals (modulus square) of the symmetry-broken “singlet” sS-UHF solution (b1), with the corresponding total electron density exhibiting non-circular shape (b2). The energy of the sS-UHF solution shows a gain of 44.3% of the correlation energy. (c) Electron density of the spin-projected (SP) singlet, showing broken spatial symmetry, but with an additional gain of correlation energy. (d) the spin-and-angular-momentum projected state (S&) exhibiting restored circular symmetry with a 73.1% gain of the correlation energy. The choice of parameters is: dielectric constant $\kappa = 8$, parabolic confinement $\omega_0 = 5$ meV, and effective mass $m^* = 0.067m_e$. Distances are in nanometers and the densities in 10^{-4} nm^{-2} .

where Ψ_{UHF} is the original symmetry-broken UHF determinant. In Eq. (4), the spin projection operator is given by

$$\mathcal{P}_{\text{spin}}(s) \equiv \prod_{s' \neq s} \frac{\hat{S}^2 - s'(s' + 1)\hbar^2}{[s(s + 1) - s'(s' + 1)]\hbar^2}, \quad (5)$$

where the index s' runs over the quantum numbers of \hat{S}^2 , with \hat{S} being the total spin.

The angular momentum projector is given by

$$2\pi\mathcal{P}_L \equiv \int_0^{2\pi} d\gamma \exp[-i\gamma(\hat{L} - L)], \quad (6)$$

where $\hat{L} = \hat{l}_1 + \hat{l}_2$ is the total angular momentum operator. As seen from Eq. (6), application of the projection operator \mathcal{P}_L to the spin-restored state $\Psi_{\text{SP}}(s)$ corresponds to a continuous configuration interaction (CCI) formalism.

In the following we focus on the ground state of the system, i.e., $L = 0$. The energy of the projected state is given by

$$E_{\text{PRJ}}(L) = \int_0^{2\pi} h(\gamma)e^{i\gamma L} d\gamma / \int_0^{2\pi} n(\gamma)e^{i\gamma L} d\gamma, \quad (7)$$

with $h(\gamma) = \langle \Psi_{\text{SP}}(s; 0) | H | \Psi_{\text{SP}}(s; \gamma) \rangle$ and $n(\gamma) = \langle \Psi_{\text{SP}}(s; 0) | \Psi_{\text{SP}}(s; \gamma) \rangle$, where $\Psi_{\text{SP}}(s; \gamma)$ is the spin-restored wave function rotated by an azimuthal angle γ and H is the many-body hamiltonian. We note that the UHF energies are simply given by $E_{\text{UHF}} = h(0)/n(0)$.

The electron densities corresponding to the initial RHF approximation [shown in Fig. 2(a)] and the final spin-and-angular-momentum projection (S&) [shown in Fig. 2(d)], are circularly symmetric, while those corresponding to the two intermediate approximations, i.e., the sS-UHF and spin-projected (SP) solutions [Figs. 2(b2) and 2(c), respectively] break the circular symmetry. This behavior illustrates graphically the meaning of the term restoration of symmetry, and the interpretation that the sS-UHF broken-symmetry solution refers to the intrinsic (rotating) frame of reference of the electron molecule. In light of this discussion the final projected state is called a *rotating Wigner molecule*, or RWM.

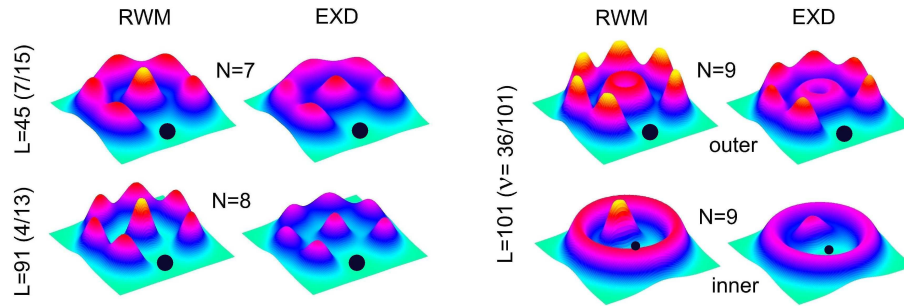


Fig. 3 Conditional probability distributions (CPDs) at high B , evaluated for parabolic quantum dots through: (i) the two-step procedure of symmetry breaking and subsequent restoration, resulting in rotating Wigner molecules (RWM) (shown in the left columns for given N), and (ii) exact diagonalization (EXD, shown in the right columns for given N). The angular momentum values, and corresponding values of the fractional filling [see Eq(8)], are given on the left. The optimal polygonal structure for a given N is given by (n_1, n_2) with $n_1 + n_2 = N$. For $N = 7, 8$, and 9 , these arrangements are $(1,6)$, $(1,7)$, and $(2,7)$, respectively. The reference point for the calculation of the CPD is denoted by a filled dot. Note in particular the two CPDs shown for $N = 9$, illustrating that for a reference point located on the outer ring, the inner ring appears uniform, and vice versa for a reference point located on the inner ring (bottom row on the right). These results illustrate that the rings rotate independently of each other.

1.2 Electrons in circular quantum dots under high magnetic fields

To illustrate the emergence of RWMs in parabolically confined QDs under high B , we show in Fig. 3 results obtained [14] through the aforementioned two-step computational technique for $N = 7, 8$, and 9 electrons, and compare them with the results derived from exact diagonalization of the Hamiltonian [see Eq(2)]. Systematic investigations of QDs under high B revealed electronic states of crystalline character. These states are found for particular “magic” angular momentum values (L) that exhibit enhanced stability and are called cusp states. For a given value of B , one of these L ’s corresponds to the global minimum, i.e., the ground state, and varying B causes the ground state and its angular momentum to change. The cusp states have been long recognized [18] as the finite- N precursors of the fractional quantum Hall states in extended systems. In particular, the fractional fillings ν (defined in the thermodynamic limit) are related to the magic angular momenta of the finite- N system as follows [19]

$$\nu = \frac{N(N-1)}{2L}. \quad (8)$$

In the literature of the fractional quantum Hall effect (FQHE), ever since the celebrated paper [20] by Laughlin in 1983, the cusp states have been considered to be the antithesis of the Wigner crystal and to be described accurately by liquid-like wave functions, such as the Jastrow- Laughlin (JL) [20, 21] and composite-fermion (CF) [22, 23] ones. This view, however, has been challenged recently [11, 12] by the explicit derivation of trial wave functions for the cusp states that are associated with a rotating Wigner molecule. As discussed elsewhere [11, 12], these parameter-free wave functions, which are by construction crystalline in character, have been shown to provide a simpler and improved description of the cusp states, in particular for high angular momenta (corresponding to low fractional fillings).

The crystalline arrangements that were found [11, 12, 13, 14] consist of concentric polygonal rings [see the conditional probabilities displayed in Fig. 3, with the reference (observation) point denoted by a filled dot]. These rings rotate independently of each other (see in particular the two cases shown for $N = 9$), with the electrons on each ring rotating coherently [14]. The rotations stabilize the RWM relative to the static one – namely, the projected (symmetry restored) states are lower in energy compared to the broken-symmetry ones (the unrestricted Hartree-Fock solutions).

1.3 Symmetry breaking of trapped bosons

In closing this section, we remark that the emergence of crystalline geometric arrangements, discussed above for electrons confined in 2D quantum dots, appears to be a general phenomenon that is predicted [24] to occur also for trapped bosonic atomic systems (neutral or charged) when the interatomic repulsion is tuned to exceed the characteristic energy of the harmonic trap. Indeed, application of the aforementioned two-step method, allowed the evaluation [24] of solutions to the many-body Hamiltonians describing such bosonic systems, going beyond the mean-field (Gross-Pitaevskii) approach. These highly-correlated trapped 2D states exhibit localization of the bosons into polygonal-ringlike crystalline patterns, thus extending earlier work that predicted localization of strongly repelling 1D bosons (often referred to as the Tonk-Girardeau regime [25, 26]), to a higher dimension. It is expected that these theoretical findings will be the subject of experimental explorations, using methodologies that have led recently to observations of localization transitions in 1D boson systems [27, 28].

2 Localization and entanglement in a two-electron elliptic quantum dot

As discussed in the previous section, electron localization leading to formation of molecular-like structures [the aforementioned Wigner molecules] within a *single circular* two-dimensional (2D) quantum dot at zero magnetic field (B) has been theoretically predicted to occur [4, 5, 7, 29, 30], as the strength of the e - e repulsive interaction relative to the zero-point energy increases. Of particular interest is a two-electron ($2e$) WM, in light of the current experimental effort [31, 32] aiming at implementation of a spin-based [33] solid-state quantum logic gate that employs two coupled one-electron QDs (double dot).

Here, we present an exact diagonalization (EXD) and an approximate (generalized Heitler-London, GHL) microscopic treatment for two electrons in a *single* elliptic QD specified by the parameters of a recently investigated experimental device [34]. While formation of Wigner molecules in circular QDs requires weak confinement, and thus large dots of lower densities (so that the interelectron repulsion dominates), we show that formation of such WMs is markedly enhanced in highly deformed (e.g., elliptic) dots due to their lower symmetry. The calculations provide a good description of the measured $J(B)$ curve (the singlet-triplet splitting) when screening [35, 36] due to the metal gates and leads is included (in addition to the weakening of the effective inter-electron repulsion due to the dielectric constant of the semiconductor, GaAs). In particular, our results reproduce the salient experimental findings pertaining to the vanishing of $J(B)$ for a finite value of $B \sim 1.3$ T [associated with a change in sign of $J(B)$ indicating a singlet-triplet (ST) transition], as well as the flattening of the $J(B)$ curve after the ST crossing. These properties, and in particular the latter one, are related directly to the formation of an electron molecular dimer and its effective dissociation for large magnetic fields. The effective dissociation of the electron dimer is most naturally described through the GHL approximation, and it is fully supported by the more accurate, but physically less transparent, EXD.

Of special interest for quantum computing is the degree of entanglement exhibited by the two-electron molecule in its singlet state [33]. Here, in relation to the microscopic calculations, we investigate two different measures of entanglement [37]. The first, known as the concurrence (C) for two *indistinguishable* fermions [38, 39], has been used in the analysis of the experiment in Ref. [34] (this measure is related to the operational cycle of a two-spin-qubit quantum logic gate [38, 39]). The second measure, referred to as the von Neumann entropy (S) for *indistinguishable* particles, has been developed in Ref. [40] and used in Ref. [41]. We show that the present *wave-function-based* methods, in conjunction with the knowledge of the dot shape and the $J(B)$ curve, enable theoretical determination of the degree of entanglement, in particular for the elliptic QD of Ref. [34]. The increase in the degree of entanglement (for both measures) with stronger magnetic fields correlates with the dissociation of the $2e$ molecule. This supports the experimental assertion [34] that cotunneling spectroscopy can probe properties of the electronic wave function of the QD, and not merely its low-energy spectrum. Our methodology can be straightforwardly applied to other cases of strongly-interacting devices, e.g., double dots with strong interdot-tunneling.

2.1 Microscopic treatment

The Hamiltonian for two 2D interacting electrons is [see Eq. (2)]

$$\mathcal{H} = H(\mathbf{r}_1) + H(\mathbf{r}_2) + e^2/(\kappa r_{12}), \quad (9)$$

where the last term is the Coulomb repulsion, κ is the dielectric constant, and $r_{12} = |\mathbf{r}_1 - \mathbf{r}_2|$. $H(\mathbf{r})$ is the single-particle Hamiltonian for an electron in an external perpendicular magnetic field \mathbf{B} and an appropriate confinement potential. When position-dependent screening is included, the last term in Eq. (9) is modified by a function of r_{12} (see below). For an elliptic QD, the single-particle Hamiltonian is written as

$$H(\mathbf{r}) = T + \frac{1}{2}m^*(\omega_x^2 x^2 + \omega_y^2 y^2) + \frac{g^*\mu_B}{\hbar}\mathbf{B} \cdot \mathbf{s}, \quad (10)$$

where $T = (\mathbf{p} - e\mathbf{A}/c)^2/2m^*$, with $\mathbf{A} = 0.5(-By, Bx, 0)$ being the vector potential in the symmetric gauge. m^* is the effective mass and \mathbf{p} is the linear momentum of the electron. The second term is the external confining potential; the last term is the Zeeman interaction with g^* being the effective g factor, μ_B the Bohr magneton, and \mathbf{s} the spin of an individual electron.

The GHL method for solving the Hamiltonian (9) consists of two steps. In the first step, we solve selfconsistently the ensuing unrestricted Hartree-Fock (UHF) equations allowing for lifting of the double-occupancy requirement (imposing this requirement gives the *restricted* HF method, RHF). For the $S_z = 0$ solution, this step produces two single-electron orbitals $u_{L,R}(\mathbf{r})$ that are localized left (L) and right (R) of the center of the QD [unlike the RHF method that gives a single doubly-occupied elliptic (and symmetric about the origin) orbital]. At this step, the many-body wave function is a single Slater determinant $\Psi_{\text{UHF}}(1 \uparrow, 2 \downarrow) \equiv |u_L(1 \uparrow)u_R(2 \downarrow)\rangle$ made out of the two occupied UHF spin-orbitals $u_L(1 \uparrow) \equiv u_L(\mathbf{r}_1)\alpha(1)$ and $u_R(2 \downarrow) \equiv u_R(\mathbf{r}_2)\beta(2)$, where $\alpha(\beta)$ denotes the up (down) [\uparrow (\downarrow)] spin. This UHF determinant is an eigenfunction of the projection S_z of the total spin $\hat{S} = \hat{s}_1 + \hat{s}_2$, but not of \hat{S}^2 (or the parity space-reflection operator).

In the second step, we restore the broken parity and total-spin symmetries by applying to the UHF determinant the projection operator [15, 42] $\mathcal{P}_{\text{spin}}^{s,t} = 1 \mp \varpi_{12}$, where the operator ϖ_{12} interchanges the spins of the two electrons [this is a special case of the operator given in Eq. (5)]; the upper (minus) sign corresponds to the singlet. The final result is a generalized Heitler-London (GHL) two-electron wave function $\Psi_{\text{GHL}}^{s,t}(\mathbf{r}_1, \mathbf{r}_2)$ for the ground-state singlet (index s) and first-excited triplet (index t), which uses the UHF localized orbitals,

$$\Psi_{\text{GHL}}^{s,t}(\mathbf{r}_1, \mathbf{r}_2) \propto (u_L(\mathbf{r}_1)u_R(\mathbf{r}_2) \pm u_L(\mathbf{r}_2)u_R(\mathbf{r}_1))\chi^{s,t}, \quad (11)$$

where $\chi^{s,t} = (\alpha(1)\beta(2) \mp \alpha(2)\beta(1))$ is the spin function for the $2e$ singlet and triplet states. The general formalism of the 2D UHF equations and of the subsequent restoration of broken spin symmetries can be found in Refs. [15, 16, 29, 42].

The use of *optimized* UHF orbitals in the GHL is suitable for treating *single elongated* QDs. The GHL is equally applicable to double QDs with arbitrary interdot-tunneling coupling [15, 42]. In contrast, the Heitler-London (HL) treatment [43] (known also as Valence bond), where non-optimized “atomic” orbitals of two isolated QDs are used, is appropriate only for the case of a double dot with small interdot-tunneling coupling [33].

The orbitals $u_{L,R}(\mathbf{r})$ are expanded in a real Cartesian harmonic-oscillator basis, i.e.,

$$u_{L,R}(\mathbf{r}) = \sum_{j=1}^K C_j^{L,R} \varphi_j(\mathbf{r}), \quad (12)$$

where the index $j \equiv (m, n)$ and $\varphi_j(\mathbf{r}) = X_m(x)Y_n(y)$, with $X_m(Y_n)$ being the eigenfunctions of the one-dimensional oscillator in the $x(y)$ direction with frequency $\omega_x(\omega_y)$. The parity operator \mathcal{P} yields

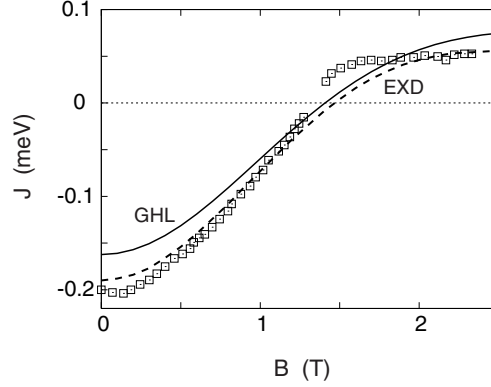


Fig. 4 The singlet-triplet splitting $J = E^s - E^t$ as a function of the magnetic field B for an elliptic QD with $\hbar\omega_x = 1.2$ meV and $\hbar\omega_y = 3.3$ meV (these values correspond to the device of Ref. [34]). Solid line: GHL (broken-symmetry UHF + restoration of symmetries) results with a coordinate-independent screening ($\kappa = 22$). Dashed line: EXD results with $\kappa = 12.9$ (GaAs), but including screening with a coordinate dependence according to Ref. [36] and $d = 18.0$ nm (see text). The rest of the material parameters used are: m^* (GaAs) = $0.067m_e$, and $g^* = 0$ (see text). The experimental measurements [34] are denoted by open squares. Our sign convention for J is opposite to that in Ref. [34].

$\mathcal{P}X_m(x) = (-1)^m X_m(x)$, and similarly for $Y_n(y)$. The expansion coefficients $C_j^{L,R}$ are real for $B = 0$ and complex for finite B . In the calculations we use $K = 79$, yielding convergent results.

In the EXD method, the many-body wave function is written as a linear superposition over the basis of non-interacting two-electron determinants, i.e.,

$$\Psi_{\text{EXD}}^{s,t}(\mathbf{r}_1, \mathbf{r}_2) = \sum_{i < j}^{2K} \Omega_{ij}^{s,t} |\psi(1; i)\psi(2; j)\rangle, \quad (13)$$

where $\psi(1; i) = \varphi_i(1 \uparrow)$ if $1 \leq i \leq K$ and $\psi(1; i) = \varphi_{i-K}(1 \downarrow)$ if $K + 1 \leq i \leq 2K$ [and similarly for $\psi(2, j)$]. The total energies $E_{\text{EXD}}^{s,t}$ and the coefficients $\Omega_{ij}^{s,t}$ are obtained through a “brute force” diagonalization of the matrix eigenvalue equation corresponding to the Hamiltonian in Eq. (9). The EXD wave function does not immediately reveal any particular form, although, our calculations below show that it can be approximated by a GHL wave function in the case of the elliptic dot under consideration.

To model the experimental elliptic QD device, we take, following Ref. [34], $\hbar\omega_x = 1.2$ meV and $\hbar\omega_y = 3.3$ meV. The effective mass of the electron is taken as $m^* = 0.067m_e$ (GaAs). Since the experiment did not resolve the lifting of the triplet degeneracy caused by the Zeeman term, we take $g^* = 0$. Using the two step method, we calculate the GHL singlet-triplet splitting $J_{\text{GHL}}(B) = E_{\text{GHL}}^s(B) - E_{\text{GHL}}^t(B)$ as a function of the magnetic field in the range $0 \leq B \leq 2.5$ T. Screening of the e - e interaction due to the metal gates and leads must be considered in order to reproduce the experimental $J(B)$ curve [44]. This screening can be modeled, to first approximation, by a position-independent adjustment of the dielectric constant κ [45]. Indeed, with $\kappa = 22.0$ (instead of the GaAs dielectric constant, i.e., $\kappa = 12.9$), good agreement with the experimental data is obtained [see Fig. 4]. In particular, we note the singlet-triplet crossing for $B \approx 1.3$ T, and the flattening of the $J(B)$ curve beyond this crossing.

We have also explored, particularly in the context of the EXD treatment, a position-dependent screening using the functional form, $(e^2/\kappa r_{12})[1 - (1 + 4d^2/r_{12}^2)^{-1/2}]$, proposed in Ref. [36], with d as a fitting parameter. The $J_{\text{EXD}}(B)$ result for $d = 18.0$ nm is depicted in Fig. 4 (dashed line), and it is in very good agreement with the experimental measurement.

The singlet state electron densities from the GHL and the EXD treatments at $B = 0$ and $B = 2.5$ T are displayed in Fig. 5. These densities illustrate the dissociation of the electron dimer with increasing

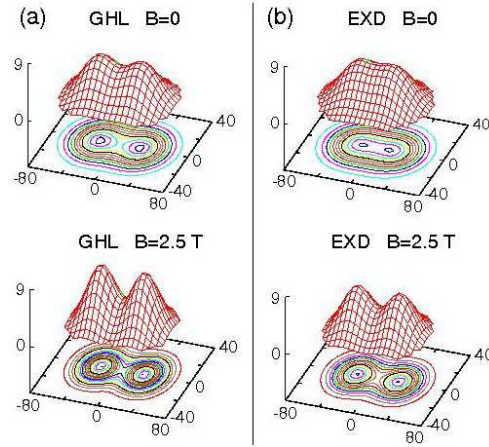


Fig. 5 Total electron densities (EDs) associated with the singlet state of the elliptic dot at $B = 0$ and $B = 2.5$ T. (a) The GHL densities. (b) The EXD densities. The rest of the parameters and the screening of the Coulomb interaction are as in Fig. 4. Lengths in nm and densities in 10^{-4} nm^{-2} .

magnetic field. The asymptotic convergence (beyond the ST point) of the energies of the singlet and triplet states, i.e., $[J(B) \rightarrow 0 \text{ as } B \rightarrow \infty]$ is a reflection of the dissociation of the $2e$ molecule, since the ground-state energy of two fully spatially separated electrons (zero overlap) does not depend on the total spin [46].

2.2 Measures of entanglement [37]

To calculate the concurrence \mathcal{C} [38, 39], one needs a decomposition of the GHL wave function into a linear superposition of *orthogonal* Slater determinants. Thus one needs to expand the *nonorthogonal* $u^{L,R}(\mathbf{r})$ orbitals as a superposition of two other *orthogonal* ones. To this effect, we write $u^{L,R}(\mathbf{r}) \propto \Phi^+(\mathbf{r}) \pm \xi \Phi^-(\mathbf{r})$, where $\Phi^+(\mathbf{r})$ and $\Phi^-(\mathbf{r})$ are the parity symmetric and antisymmetric (along the x -axis) components in their expansion given by Eq. (12). Subsequently, with the use of Eq. (11), the GHL singlet can be rearranged as follows:

$$\Psi_{\text{GHL}}^s \propto |\Phi^+(1 \uparrow) \Phi^+(2 \downarrow)\rangle - \eta |\Phi^-(1 \uparrow) \Phi^-(2 \downarrow)\rangle, \quad (14)$$

where the so-called interaction parameter [39], $\eta = \xi^2$, is the coefficient in front of the second determinant. Knowing η allows a direct evaluation of the concurrence of the singlet state, since $\mathcal{C}^s = 2\eta/(1 + \eta^2)$ [39]. Note that $\Phi^+(\mathbf{r})$ and $\Phi^-(\mathbf{r})$ are properly normalized. It is straightforward to show that $\eta = (1 - |S_{LR}|)/(1 + |S_{LR}|)$, where S_{LR} (with $|S_{LR}| \leq 1$) is the overlap of the original $u^{L,R}(\mathbf{r})$ orbitals.

For the GHL triplet, one obtains an expression independent of the interaction parameter η , i.e.,

$$\Psi_{\text{GHL}}^t \propto |\Phi^+(1 \uparrow) \Phi^-(2 \downarrow)\rangle + |\Phi^+(1 \downarrow) \Phi^-(2 \uparrow)\rangle, \quad (15)$$

which is a maximally ($\mathcal{C}^t = 1$) entangled state. Note that underlying the analysis of the experiments in Ref. [34] is a *conjecture* that wave functions of the form given in Eqs. (14) and (15) describe the two electrons in the elliptic QD.

For the GHL singlet, using the overlaps of the left and right orbitals, we find that starting with $\eta = 0.46$ ($\mathcal{C}^s = 0.76$) at $B = 0$, the interaction parameter (singlet-state concurrence) increases monotonically to $\eta = 0.65$ ($\mathcal{C}^s = 0.92$) at $B = 2.5$ T. At the intermediate value corresponding to the ST transition ($B = 1.3$ T), we find $\eta = 0.54$ ($\mathcal{C}^s = 0.83$) [47]. Our $B = 0$ theoretical results for η and \mathcal{C}^s are in remarkable

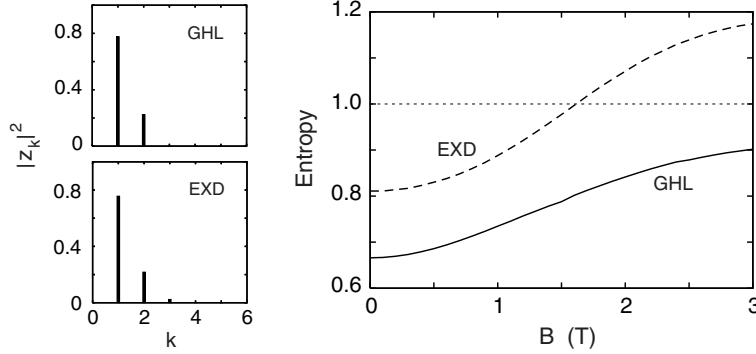


Fig. 6 Von Neumann entropy for the singlet state of the elliptic dot as a function of the magnetic field B . Solid line: GHL. Dashed line: EXD. The rest of the parameters and the screening of the Coulomb interaction are as in Fig. 4. On the left, we show histograms for the $|z_k|^2$ coefficients [see Eq. (16)] of the singlet state at $B = 1.3$ T, illustrating the dominance of two configurations. Note the small third coefficient $|z_3|^2 = 0.023$ in the EXD case.

agreement with the experimental estimates [34] of $\eta = 0.5 \pm 0.1$ and $C^s = 0.8$, which were based solely on conductance measurements below the ST transition (i.e., near $B = 0$).

To compute the von Neumann entropy, one needs to bring both the EXD and the GHL wave functions into a diagonal form (the so-called “canonical form” [40, 48]), i.e.,

$$\Psi_{\text{EXD}}^{s,t}(\mathbf{r}_1, \mathbf{r}_2) = \sum_{k=1}^M z_k^{s,t} |\Phi(1; 2k-1)\Phi(2; 2k)\rangle, \quad (16)$$

with the $\Phi(i)$'s being appropriate spin orbitals resulting from a unitary transformation of the basis spin orbitals $\psi(j)$'s [see Eq. (13)]; only terms with $z_k \neq 0$ contribute. The upper bound M can be smaller (but not larger) than K (the dimension of the single-particle basis); M is referred to as the Slater rank. One obtains the coefficients of the canonical expansion from the fact that the $|z_k|^2$ are eigenvalues of the hermitian matrix $\Omega^\dagger \Omega$ [Ω , see Eq. (13), is antisymmetric]. The von Neumann entropy is given by $\mathcal{S} = -\sum_{k=1}^M |z_k|^2 \log_2(|z_k|^2)$ with the normalization $\sum_{k=1}^M |z_k|^2 = 1$. Note that the GHL wave functions in Eqs. (14) and (15) are already in canonical form, which shows that they always have a Slater rank of $M = 2$. One finds $\mathcal{S}_{\text{GHL}}^s = \log_2(1 + \eta^2) - \eta^2 \log_2(\eta^2)/(1 + \eta^2)$, and $\mathcal{S}_{\text{GHL}}^t = 1$ for all B . For large B , the overlap between the two electrons of the dissociated dimer vanishes, and thus $\eta \rightarrow 1$ and $\mathcal{S}_{\text{GHL}}^s \rightarrow 1$.

Since the EXD singlet has obviously a Slater rank $M > 2$, the definition of concurrence is not applicable to it. The von Neumann entropy for the EXD singlet ($\mathcal{S}_{\text{EXD}}^s$) is displayed in Fig. 6, along with that ($\mathcal{S}_{\text{GHL}}^s$) of the GHL singlet. $\mathcal{S}_{\text{EXD}}^s$ and $\mathcal{S}_{\text{GHL}}^s$ are rather close to each other for the entire B range, and it is remarkable that both remain close to unity for large B , although the maximum allowed mathematical value is $\log_2(K)$ [as aforementioned we use $K = 79$, i.e., $\log_2(79) = 6.3$]; this maximal value applies for both the EXD and GHL approaches. The saturation of the entropy for large B to a value close to unity reflects the dominant (and roughly equal at large B) weight of two configurations in the canonical expansion [see Eq. (16)] of the EXD wave function, which are related to the two terms ($M = 2$) in the canonical expansion of the GHL singlet [Eq. (14)]. This is illustrated by the histograms of the $|z_k^s|^2$ coefficients for $B = 1.3$ T in Fig. 6 (left column). These observations support the GHL approximation, which is computationally less demanding than the exact diagonalization, and can be used easily for larger N .

3 Summary

We discussed symmetry breaking in two-dimensional quantum dots resulting from strong interelectron repulsion relative to the zero-point kinetic energy associated with the confining potential. Such symmetry

breaking leads to the emergence of crystalline arrangements of electrons in the dot. The so-called Wigner molecules form already at field-free conditions. The appearance of rotating Wigner molecules in circular dots under high magnetic field, and their relation to magic angular momenta and quantum-Hall-effect fractional fillings was also discussed.

Furthermore, we have shown, through exact and approximate microscopic treatments, formation of an electron molecular dimer in an elliptic QD (Fig. 5) for screened interelectron repulsion. The formation and effective dissociation (in high magnetic fields) of the electron dimer are reflected in the behavior of the computed singlet-triplet splitting, $J(B)$, that agrees well (see Fig. 4) with the measurements [34]. Furthermore, we showed that, from a knowledge of the dot shape and of $J(B)$, theoretical analysis along the lines introduced here allows probing of the correlated ground-state wave function and determination of its degree of entanglement. This presents an alternative to the experimental study where determination of the concurrence utilized conductance data [34]. We have employed two measures of entanglement for *indistinguishable fermions* (the concurrence and the von Neumann entropy) and have shown that their behavior correlates with the effective dissociation of the electron dimer. Such information is of interest to the implementation of spin-based solid-state quantum logic gates.

This research is supported by the US D.O.E. (Grant No. FG05-86ER45234), and NSF (Grant No. DMR-0205328). We thank M. Pustilnik for comments on the manuscript.

References

- [1] M.A. Kastner, *Physics Today* **46**, 24 (1993).
- [2] S. Tarucha *et al.* *Phys. Rev. Lett.* **77**, 3613 (1996).
- [3] R.C. Ashoori, *Nature* **379**, 413 (1996).
- [4] C. Yannouleas and U. Landman, *Phys. Rev. Lett.* **82**, 5325 (1999); **85**, E2220 (2000).
- [5] C. Yannouleas and U. Landman, *Phys. Rev. B* **61**, 15895 (2000).
- [6] E. Wigner, *Phys. Rev.* **46**, 1002 (1934).
- [7] C. Yannouleas and U. Landman, *Phys. Rev. Lett.* **85**, 1726 (2000).
- [8] M.E. Kellman and D.R. Herrick, *Phys. Rev. A* **22**, 1536 (1980).
- [9] M.E. Kellman, *Int. J. Quantum Chem.* **65**, 399 (1997).
- [10] R.S. Berry, *Contemp. Phys.* **30**, 1 (1989).
- [11] C. Yannouleas and U. Landman, *Phys. Rev. B* **66**, 115315 (2002).
- [12] C. Yannouleas and U. Landman, *Phys. Rev. B* **68**, 035326 (2003).
- [13] C. Yannouleas and U. Landman, *Phys. Rev. B* **69**, 113306 (2004).
- [14] C. Yannouleas and U. Landman, *Phys. Rev. B* **70**, 235319 (2004).
- [15] C. Yannouleas and U. Landman, *Int. J. Quantum Chem.* **90**, 699 (2002).
- [16] C. Yannouleas and U. Landman, *J. Phys.: Condens. Matter* **14**, L591 (2002).
- [17] P.O. Löwdin, *Rev. Mod. Phys.* **36**, 966 (1964).
- [18] R.B. Laughlin, *Phys. Rev. B* **27**, 3383 (1983).
- [19] S.M. Girvin and T. Jach, *Phys. Rev. B* **28**, 4506 (1983).
- [20] R.B. Laughlin, *Phys. Rev. Lett.* **50**, 1395 (1983).
- [21] R.B. Laughlin, in: *The Quantum Hall Effect*, edited by R.E. Prange and S.M. Girvin (Springer, New York, 1987), p. 233.
- [22] J.K. Jain, *Phys. Rev. B* **41**, 7653 (1990).
- [23] S.S. Mandal, M.R. Peterson, and J.K. Jain, *Phys. Rev. Lett.* **90**, 106403 (2003).
- [24] I. Romanovsky, C. Yannouleas, and U. Landman, *Phys. Rev. Lett.* **93**, 230405 (2004).
- [25] M. Girardeau, *J. Math. Phys.* **1**, 516 (1960).
- [26] M.D. Girardeau and E.M. Wright, *Laser Phys.* **12**, 8 (2002).
- [27] B. Paredes *et al.*, *Nature* **429**, 277 (2004).
- [28] G.T. Kinoshita, T. Wenger, and D.S. Weiss, *Science* **305**, 1125 (2004).
- [29] C. Yannouleas and U. Landman, *Phys. Rev. B* **68**, 035325 (2003).
- [30] S.A. Mikhailov, *Phys. Rev. B* **65**, 115312 (2002).
- [31] J.M. Elzerman *et al.*, *Lect. Notes Phys.* **667**, 25 (2005), edited by W.D. Heiss (Springer, Berlin, 2005).
- [32] H.A. Engel *et al.*, *Quantum Information Processing* **3**, 115 (2004).
- [33] G. Burkard, D. Loss, and D.P. DiVincenzo, *Phys. Rev. B* **59**, 2070 (1999).
- [34] D.M. Zumbühl *et al.*, *Phys. Rev. Lett.* **93**, 256801 (2004).

- [35] S. Tarucha, D.G. Austing, Y. Tokura, W.G. van der Wiel, and L.P. Kouwenhoven, Phys. Rev. Lett. **84**, 2485 (2000).
- [36] L.D. Hallam, J. Weis, and P.A. Maksym, Phys. Rev. B **53**, 1452 (1996).
- [37] Various approaches for estimating the degree of entanglement have been proposed, including schemes which apply for *distinguishable* [see e.g., W.K. Wootters, Phys. Rev. Lett. **80**, 2245 (1998)] or *indistinguishable* particles, with only the latter being relevant in our case. For a review, see K. Eckert *et al.*, Ann. of Phys. (NY) **299**, 88 (2002); for the consequences of indistinguishability, see section 2.2 therein.
- [38] J. Schliemann, D. Loss, and A.H. MacDonald, Phys. Rev. B **63**, 085311 (2001).
- [39] V.N. Golovach and D. Loss, Phys. Rev. B **69**, 245327 (2004).
- [40] R. Paskauskas and L. You, Phys. Rev. A **64**, 042310 (2001).
- [41] L. Xe, G. Bester, and A. Zunger, cond-mat/0503492
- [42] C. Yannouleas and U. Landman, Eur. Phys. J. D **16**, 373 (2001).
- [43] H. Heitler and F. London, Z. Phys. **44**, 455 (1927).
- [44] This is in agreement with the analysis of the only other measured $J(B)$ curve in a different device [45], where the $J(B)$ curve was measured *before* the singlet-triplet crossing.
- [45] J. Kyriakidis *et al.*, Phys. Rev. B **66**, 035320 (2002)].
- [46] In contrast, the singlet-state RHF electron densities fail to exhibit formation of an electron dimer for all values of B . This underlies the failure of the RHF method to describe the behavior of the experimental $J(B)$ curve. In particular, $J_{\text{RHF}}(B = 0)$ has the wrong sign, while $J_{\text{RHF}}(B)$ diverges for high B as is the case for the RHF treatment of double dots (see Ref. [15, 42]).
- [47] For the RHF, $C_{\text{RHF}}^s = 0$, since a single determinant is unentangled for both the two measures considered here.
- [48] J. Schliemann *et al.*, Phys. Rev. A **64**, 022303 (2001).